nature water

Article

https://doi.org/10.1038/s44221-023-00180-8

Multifunctional zwitterionic hydrogels for the rapid elimination of organic and inorganic micropollutants from water

In the format provided by the authors and unedited

Table of Contents

1. Supplementary Discussion

1.1 Isotherm shape, maximum absorption capacity, and saturation

The capacity of any absorbent or adsorbent is, in general, governed by the Langmuir isotherm or a similar isotherm. These isotherms have two limiting regimes:

(1) At low supernatant concentrations c_{out} relative to the number of active sites, these isotherms reduce to a linear form for the concentration of absorbed micropollutant $c_{in} = Kc_{out}$, where K is the partition coefficient. In this case, the supernatant concentration limits micropollutant uptake by the absorbent or adsorbent.
(2) At high supernatant concentrations, the concentration of absorbed micropollutant is limited by the number of active sites available for micropollutant uptake, and $c_{in} \to a$, the number of active sites per unit volume.

At a typical internal concentration of absorbed micropollutants of 10 ppm (figure 2), the moles of micropollutant absorbed per microparticle are of the order of 10^{-12}, over 3 orders of magnitude lower than the estimated number of active absorbing molecules (supplementary information 1.2). As such, we operate the hydrogels exclusively in the first limiting regime, and the isotherms have a linear shape (figure 1). In this regime, saturation is limited solely by the supernatant concentration c_{out}. Using a mass balance, the capacity at saturation for a batch process is given by:

$$Capacity\ \left(\frac{w}{w}\right) = \frac{KV_p c_0}{\rho\left(V + V_p K\right)} \tag{1.1.1}$$

Where c_0 is the initial micropollutant concentration (g/L) in the supernatant, V is the volume of water treated, V_p is the volume of hydrogel, and ρ is its density. For a continuous process, like the packed bed filter in figure 4,

$$Capacity\ \left(\frac{w}{w}\right) = \frac{Kc_0}{\rho} \tag{1.1.2}$$

The hydrogels do have a maximum absorption capacity independent of supernatant concentration, which may determined using the method of supplementary information 1.2, but these limits are never approached at environmentally relevant concentrations (or indeed, for any concentrations for organic micropollutants which have limited solubility).

1.2 Estimation of the number of moles of active molecules per microparticle

	Added to 10 ml soln. (g)	Added to 10 ml soln. (mol)	Attachment fraction	Functional moles reacted	Moles after washing	Moles per cc	Moles per particle
PSB	5.65	2.02E-02	0.968	1.96E-02	1.59E-02	1.59E-03	1.12E-07
DTPA-AA	–	1.00E-03	1.000	1.00E-03	8.12E-04	8.12E-05	5.72E-09
F127DA	3	2.36E-04	0.989	2.34E-04	1.90E-04	1.90E-05	1.34E-09

Table 1 | Estimated number of moles of molecules active in absorption per microparticle.

As shown in table 1, we start with the mass or number of moles of the functional molecules added to 10 ml of monomer solution as described in the methods section. DTPA-AA and F127DA are synthesized from a chelating agent (DTPA-DA) and surfactant (Pluronic F127) that do not possess double bonds to enable their incorporation into the hydrogel. The synthesis process does not have a perfect yield, and we must reduce the added quantity by molecules which do not possess even a single double bond. At the same time, the conversion in the polymerization process is not perfect either, and the added quantity must also be corrected by this yield. To correct for these effects and obtain the functional moles reacted, the added amount is scaled by an attachment fraction f, which is the fraction of molecules with at least one double bond moiety, which is converted during the polymerization reaction. If the yield of the first functionalization reaction is p_1, the yield of the second polymerization reaction is p_2, and total number of sites that can be functionalized per non-functional precursor is N, then it can be seen that:

$$f = \sum_{i=1}^{N} \binom{N}{i} p_1^i (1-p_1)^{N-i} \left[1-(1-p_2)^i\right] \tag{1.2.1}$$

We assume that p_1 and p_2 are identical for all reactants since that is the only form in which this information can be obtained experimentally (using 1H-NMR), i.e. all reacting sites have equal reactivity. In prior work, we showed that for similar hydrogels using the same reaction setup, $p_2 = 0.968$ [1]. Similarly, from 1H-NMR data (supplementary figure S13), $p_{1,F127DA} = 0.923$, and $p_{1,DTPA-AA} = 0.980$. After scaling by f to obtain the number of reacted active molecules, these are then scaled down for losses during the washing process (18.8%) [1].

Finally, we determine the volume of each particle at synthesis and use it to determine the moles of active molecules per particle, starting from the equilibrium swollen size of the hydrogel microparticles in water, about 800 µm. Using the data in table 2, this corresponds to a size at synthesis of:

$$d_{synthesis} = d_{swollen}\left(\frac{V_{original}}{V_{swollen}}\right)^{\frac{1}{3}}$$

For a single particle, this equation yields: $d_{synthesis} = 512\ \mu m$, $V_{synthesis} = 7.04 \times 10^{-5} cm^3$, which can be used to obtain the final result in table 1. It must be noted that these values are estimates, expected to be accurate to within an order of magnitude.

1.3 Comparison with alginate microparticles

Alginates are of potential interest in removing metals from water due to their ability to form egg-shell structures that effectively chelate ions[2]. Metal ions form bridges between the alginate chains and act as physical crosslinks, leading to gel formation. However, it is well known that alginates fall apart in salt water, and therefore cannot be used in real water treatment applications[3]. Inspired by recent work to improve the toughness of alginates, we prepare a modified alginate bearing an acrylate moiety (GMA-Alg) that makes it photocrosslinkable and resistant to salt water. The synthesis of GMA-Alg is described in supplementary information 1.4, and the structure is shown in supplementary figure S1. We then prepare hydrogel microparticles using GMA-Alg and test them as described in the main manuscript. The results of this comparative study are shown in supplementary figure S8.

1.4 Mesh size estimates

The precise determination of mesh size can be performed using Canal-Peppas (or similar) equilibrium swelling theories [4,5], dynamic light scattering, X-ray, or neutron scattering experiments [6-8], by studying partitioning of fluorescent probe molecules [9], or using simulations.

Our hydrogels are absorbents with strong interactions between micropollutants and the hydrogel matrix. Therefore, a fluorescent probe approach cannot be used to accurately obtain the mesh size. Similarly, due to the opacity of our hydrogel (supplementary figure S3(a)), dynamic light scattering approaches are not suitable. The low X-ray/neutron scattering contrast between the different components of the hydrogel among themselves and with respect to water also render a method based on WAXS or SANS infeasible. Contrast cannot be enhanced by using doping the solvent with salts like cesium chloride, since this strongly affects the structure of the gel at the concentrations necessary to achieve good contrast. Further, the presence of large micelles (~10-100 nm) within the hydrogel will confound data that might be obtained. Simulations also cannot effectively model the formation of such hydrogels at relevant length scales (~100 nm) while reproducing accurate mesh size values.

Therefore, we are left with theoretical approaches based on swelling to determine the mesh size, requiring knowledge of several chemical parameters, such as the Flory characteristic ratio C_∞, the junction functionality f, the degree of polymerization between junctions N_j, the repeating unit average bond length l, the number of carbon-carbon bonds per repeating unit λ, and the swollen polymer volume fraction ϕ_s, among others, based on the form of the equation used. Our hydrogels are chemically complex materials consisting of multiple monomers, and the values used should be appropriately averaged quantities, but current theory does not address such materials, especially when certain components (micelles) have a tendency to self-assemble before and during hydrogel formation.

We therefore choose to neglect the effect of micelles and chelating agents in the values of parameters used to estimate the mesh size, except for any indirect influences through the use of

swelling data (supplementary information 2.1) measured using hydrogels that do contain micelles and chelating agents. We use two approaches to estimate the mesh size of non-zwitterionic (PEGDA) and zwitterionic (PSB) hydrogels, as described in references [4,5]. Reference [4] presents the classical Canal-Peppas theory and evaluates mesh size as:

$$\xi = \phi_s^{-\frac{1}{3}} l \left(2 C_\infty N_j\right)^{\frac{1}{2}} \tag{1.4.1}$$

Reference [5] corrects for the effects of junction functionality:

$$\xi = \phi_s^{-\frac{1}{3}} l \left(\left(1 - \frac{2}{f}\right) C_\infty \lambda N_j\right)^{\frac{1}{2}} \tag{1.4.2}$$

	Non-zwitterionic hydrogel	**Zwitterionic hydrogel**	**Difference (%)**
$\boldsymbol{\phi_s}$ (from section 2.1)	0.0692	0.0377	
$\boldsymbol{l}$	0.15	0.154	
$\boldsymbol{f}$	4	4	
$\boldsymbol{C_\infty}$	4	8.1	
$\boldsymbol{\lambda}$	3	2	
$\boldsymbol{N_j}$	13	13	
Canal-Peppas [4] mesh size (nm)	3.73	6.67	78.82
Richbourg-Peppas [5] mesh size (nm)	3.23	4.71	45.82

Table 2 | Estimated mesh sizes of non-zwitterionic and zwitterionic hydrogels.

As can be seen in table 2, the mesh size of zwitterionic hydrogels is estimated to be significantly larger than the non-zwitterionic hydrogels. More conclusively, we observed that when non-zwitterionic and zwitterionic hydrogels tablets were synthesized to have the same cross-linking density and degree of polymerization between junctions at synthesis, the zwitterionic hydrogel tablet reached a higher degree of swelling than the non-zwitterionic hydrogel. The greater swelling implies that the zwitterionic hydrogel must have a larger mesh size than the non-zwitterionic hydrogel as described in supplementary information 2.1. It may also be noted that the zwitterionic hydrogel mesh size estimate is more significantly affected by the junction functionality correction due to its larger characteristic ratio C_∞.

1.5 Analysis of FRAP (fluorescence recovery after photobleaching) intensity data

Intensity within the bleached region is governed by two competing processes – increasing intensity due to diffusion of unbleached dye into the bleached region, and continuous photobleaching due to the imaging process [10]. To correct for the effect of continuous photobleaching, a region equal in size to the bleached region is selected away from the bleached region, and the average intensity within that region is subtracted from the average intensity within the bleached region. Finally, the data is normalized so that it ranges between 0 and 1, and an exponential is fit to the data to extract a rate constant (supplementary figure S12). This rate constant obtained after normalizing the data is in the range of mass transfer coefficients associated with micropollutant uptake shown in figure 3(d). ($k = 0.5960 \pm 0.0053$ min^{-1})

$$I_{norm}(t) = \frac{[I_{bleach}(t) - I_{unbleach}(t)] - [I_{bleach}(0) - I_{unbleach}(0)]}{[I_{bleach}(+\infty) - I_{unbleach}(+\infty)] - [I_{bleach}(0) - I_{unbleach}(0)]} \tag{1.5.1}$$

$$I_{norm}(t) = 1 - e^{-kt} \tag{1.5.2}$$

1.6 Analysis of kinetics data

Let c be the pollutant concentration in solution at time t, with initial value c_0. K is the partition coefficient, $k_c a$ is the mass transfer coefficient, and c_s is the concentration at time t in the solution equilibrium which is in equilibrium with the concentration inside the microparticle. Let the average concentration inside the particles be q. V is the volume of the supernatant and V_p is the volume of the particles. Then, we have the following equations based on equilibrium, mass transfer and pollutant mass balance respectively.

$$q = Kc_s \tag{1.6.1}$$

$$\frac{dc}{dt} = k_c a(c - c_s) \tag{1.6.2}$$

$$q = \frac{V}{V_p}(c_0 - c) \tag{1.6.3}$$

Combining these, we get

$$\frac{dc}{dt} = k_c a\left(\left(1 + \frac{V}{V_p K}\right)c - \frac{V}{V_p K}c_0\right)$$

Solving this differential equation for $c(t)$, with initial condition $c(0) = c_0$ yields

$$\frac{c(t)}{c_0} = \frac{\frac{V}{V_p K} + e^{-\left(1+\frac{V}{V_p K}\right)k_c a t}}{\frac{V}{V_p K} + 1}$$

Let the dimensionless group $\alpha = V/V_p K$,

$$\frac{c(t)}{c_0} = \frac{\alpha + e^{-(1+\alpha)k_c a t}}{1+\alpha} \tag{1.6.4}$$

This equation can be fit to the data in figure 3 and used to obtain the mass transfer coefficients $k_c a$. For this purpose, we define fitting parameters,

$$\phi_1 = \frac{\alpha}{1+\alpha} \tag{1.6.5}$$

$$\phi_2 = (1+\alpha)k_c a \tag{1.6.6}$$

And fit the data shown in figure 3(a,c) to the equation,

$$\frac{c(t)}{c_0} = \phi_1 + (1-\phi_1)e^{-\phi_2 t}$$

Mass transfer coefficients are obtained as

$$k_c a = (1-\phi_1)\phi_2 \tag{1.6.7}$$

At equilibrium,

$$c_\infty = \phi_1 c_0 = \frac{\alpha c_0}{1+\alpha} \tag{1.6.8}$$

$$q_\infty = K c_\infty = \frac{K\alpha c_0}{1+\alpha} \tag{1.6.9}$$

It is also possible to use kinetics data to obtain effective diffusion coefficients for the transport of micropollutants within the hydrogel microparticles as described in ref. [11, 12]. If $q(r,t)$ is the local concentration of a micropollutant within each of the N microparticles of radius R, the transport of that micropollutant is governed by the diffusion equation for radial transport in spherical coordinates,

$$\frac{\partial q(r,t)}{\partial t} = D\nabla^2 q(r,t) = \frac{D}{r^2}\frac{\partial}{\partial r}\left(r^2 \frac{\partial q(r,t)}{\partial r}\right) \tag{1.6.10}$$

Here, D is the effective mean-field diffusion coefficient of a micropollutant in the presence of other micropollutants and the various functional groups present inside the hydrogel. The diluteness of micropollutants allows us to assume that D for a micropollutant is independent of the local concentrations of other micropollutants, and therefore is not a function of position or time within the hydrogel. The equation is subject to the initial condition,

$$q(r,0) = 0 \tag{1.6.11}$$

And boundary conditions,

$$\frac{\partial q}{\partial r}(0,t) = 0 \tag{1.6.12}$$

$$4\pi R^2 N D \frac{\partial q}{\partial r}(R,t) = V\frac{\partial c}{\partial t}(R,t) = \frac{V}{K}\frac{\partial q}{\partial t}(R,t) \tag{1.6.13}$$

The first boundary condition equation 1.6.12 is implied by symmetry, while the second equation 1.6.13 is a local instantaneous mass balance that equates the rate of mass transfer into the microparticles to the rate of decrease of micropollutant concentration in the supernatant. Here we assume that the supernatant is well-mixed. The second boundary condition may be re-cast as,

$$D\frac{\partial q}{\partial r}(R,t) = \frac{\alpha R}{3}\frac{\partial q}{\partial t}$$

Solving this system of equations, we get,

$$\frac{q(t)}{q_\infty} = 1 - \sum_{n=1}^{+\infty} \frac{6\alpha(1+\alpha)}{9(1+\alpha)+\alpha^2 s_n^2} e^{-\frac{s_n^2 D t}{R^2}} \tag{1.6.14}$$

Here, q is once again the average concentration inside the microparticle, and s_n are the increasing positive roots of the equation,

$$\tan s_n = \frac{3s_n}{3+\alpha s_n^2} \tag{1.6.15}$$

Simplifying, we get,

$$\frac{c(t)}{c_0} = \frac{\alpha + \sum_{n=1}^{+\infty} \frac{6\alpha(1+\alpha)}{9(1+\alpha)+\alpha^2 s_n^2} e^{-\frac{s_n^2 D t}{R^2}}}{1+\alpha} \tag{1.6.16}$$

Values of s_n for typical values of α are shown in ref. [11] and increase rapidly with n. Interestingly, equation 1.6.16 and the empirical equation 1.6.4 have the same form, despite equation 1.6.4 being based on a highly simplified model. Only one time scale is observed in the experimental data in figure 3(a,c). Clearly, this must be the time scale in the dominant exponent in 1.6.16, with s_1 representing the smallest non-zero root of 1.6.15. This yields,

$$\frac{s_1^2 D}{R^2} = (1+\alpha)k_c a$$

In terms of fitting parameters and constants,

$$D = \frac{\phi_2 R^2}{s_1^2} \tag{1.6.17}$$

Values of D are shown in table 3, and follow the same trends as mass transfer coefficients in figure 3(c).

Micropollutant	D (x10^{-12} m^2/s)
Pb	62.1 ± 21.2
Fe	236.3 ± 72.6
Cu	126.7 ± 38.3
EDOL	3.9 ± 1.4
BPA	1.9 ± 0.5
NOL	2.1 ± 0.7

Table 3 | Estimated effective diffusion coefficient for the absorption of micropollutants from a complex mixture into zwitterionic hydrogel microparticles.

1.7 Filter lifetime and scale up

As shown in figure 4, 2 g hydrogel cleans 2 L of water over 14 days (at a 400 ppb/contaminant contamination level). The total volume of water cleaned scales linearly with the amount of hydrogel used in the filter, for the same residence time (here, 20 min). So, we can scale the filter for operation at two length scales while retaining performance:

(1) A 500 g hydrogel filter (with a volume of about 500 ml, a common size for a household water treatment system) will clean 500 L (or 36 L/day) with a lifetime of 14 days, or 16 L/day (with intermittent usage to reduce flow and extend life) with a lifetime of 1 month. 16 L/day (which is 1 gallon/(person·day) = 4 L/(person·day) for a family of four) is a commonly accepted value for household drinking water consumption [13]. Families will be able to operate hydrogel filters for a month before they need to be replaced or regenerated.
(2) A 20 MT (metric ton) city-scale filter which cleans approximately 1 MGD (million gallons per day) of water for 14 days before it needs to be regenerated (figure 4).

The lifetime of the filters is different for individual components, and can be obtained for any specific micropollutant by using the breakthrough curve data in supplementary figure S15 scaled as described in this section.

1.8 Predicting breakthrough in microparticle-containing packed beds

With respect to a given micropollutant, breakthrough is complete, and the bed loses all ability to absorb that micropollutant when the entire bed has been saturated with that micropollutant. Bed saturation occurs when the absorbed micropollutant is in equilibrium with the inlet concentration of the micropollutant. Therefore, at the end of bed life, the total amount of micropollutant absorbed:

$$V_{hydrogel} c_{absorbed} = V_{hydrogel} K c_0$$

Where c_0 is the concentration at the inlet and K is the partition coefficient. To remove this amount of micropollutant from water in which its concentration is c_0, the volume of water that needs to have been cleaned is:

$$V_{water} = \frac{V_{hydrogel} c_{absorbed}}{c_0} = V_{hydrogel} K$$

This yields the volume of water cleaned at the end of bed life for any given micropollutant.

$$\frac{V_{water}}{V_{hydrogel}} = K \tag{1.8.1}$$

On the other hand, breakthrough begins and performance starts decreasing before this volume of water has been treated. If the residence time of the bed is τ_{bed} and the time it takes for the hydrogel microparticles to equilibrate with the given micropollutant is τ_{eq}, then breakthrough begins when that initial portion of the bed which has a residence time of $\tau_{bed} - \tau_{eq}$ has been saturated with the micropollutant. This implies:

$$V_{water} c_0 = \left(1 - \frac{\tau_{eq}}{\tau_{bed}}\right) V_{hydrogel} K c_0$$

$$\frac{V_{water}}{V_{hydrogel}} = \left(1 - \frac{\tau_{eq}}{\tau_{bed}}\right) K \tag{1.8.2}$$

The pre-factor in equation 1.8.2 depends on multiple parameters, such as the flow rate, the volume of the bed, the packing fraction (which is a function also of the compression of the hydrogels when the bed is pressurized by fluid flow), and the mass transfer coefficient of the micropollutant at the relevant flow conditions.

It is generally desirable to have $\tau_{bed} \gg \tau_{eq}$, so that the micropollutants reach equilibrium inside the bed and breakthrough starts as late as possible. When $\tau_{bed} \gg \tau_{eq}$, K is a good predictor of breakthrough. As seen from figure 3, the residence time of our packed bed (20 min) is much longer than the time needed by most micropollutants in water to equilibrate with those inside the hydrogel microparticles. As such, the partition coefficients K are a good proxy for the order in which micropollutants will pass through the column without being treated, and the value of K in figure 1(g,h) (see source data) is a good first approximation for the point $V_{water}/V_{hydrogel}$ on the x-axis in supplementary figure S15 at which performance falls off. K itself is a strong function of solubility for organic micropollutants, and of binding energy for inorganic micropollutants. Filter life can be extended and breakthrough postponed by increasing the mass of hydrogel in the bed ($V_{hydrogel}$ in equation 1.8.2).

2. Supplementary Methods

2.1 Measurement of hydrogel swelling ratios

To study the effect of using zwitterionic monomers on hydrogel mesh size, we prepared two monomer solutions:

(1) Zwitterionic hydrogel: 5.65 g PSB, 0.25 g BIS, 3.0 g F127DA, 5 ml DTPA-AA (0.25 M), 4.5 ml ethanol, and 0.5 ml PI
(2) Non-zwitterionic hydrogel: 1 ml PEGDA 700, 3.0 g F127DA, 4 ml DTPA-AA (0.25 M), 4.5 ml ethanol, and 0.5 ml PI

The compositions of these solutions are selected so that the zwitterionic and non-zwitterionic hydrogel have the same crosslinking density and the same average chain length between crosslinks, allowing for comparison on a uniform basis. The monomer solutions were poured into Petri dishes and exposed to UV light (365 nm) for 5 min to prepare two cylindrical hydrogel tablets, 3.5 cm in diameter, and 5 mm in height. The original mass of these tablets was recorded and they were immersed in excess deionized water for 24 hours, followed by a second immersion in fresh deionized water for another 24 hours to allow them to reach a swollen equilibrium. Dimensions and masses of the swollen state were recorded. The hydrogel tablets were subsequently dried in an oven, first at 70°C for 6 hours, then at 70°C under a vacuum for 6 hours, and finally at 105°C for 36 hours. The dimensions and masses of the dry state were also recorded. All dimensions and masses are shown in table 4 and are used to calculate the swelling ratio, which is a proxy for the mesh size of these hydrogels.

	Zwitterionic hydrogel			**Non-zwitterionic hydrogel**		
	Original	*Dry*	*Swollen*	*Original*	*Dry*	*Swollen*
H (cm)	0.5	0.2	0.8	0.5	0.3	0.5
D (cm)	3.5	2.1	5.4	3.5	1.7	5.0
Mass (g)	4.82	0.76	18.69	3.29	0.43	5.30
V (cc)	4.81	0.69	18.32	4.81	0.68	9.82
Density (g/cc)	1.00	1.10	1.02	0.68	0.63	0.54

Table 4 | Dimensions and masses of cylindrical non-zwitterionic and zwitterionic hydrogel tablets in various states of hydration.

Using these values, we compute two swelling ratios, which are shown in table 5.

$$Q = \frac{V_{swollen}}{V_{dry}} - 1 \tag{2.1.1}$$

$$q = \frac{m_{swollen}}{m_{dry}} - 1 \tag{2.1.2}$$

	Zwitterionic hydrogel	Non-zwitterionic hydrogel
Q	25.45	13.42
q	23.59	11.33

Table 5 | Swelling ratios of non-zwitterionic and zwitterionic hydrogels.

We observed that when non-zwitterionic and zwitterionic hydrogels tablets were synthesized to have the same cross-linking density and degree of polymerization between junctions at synthesis, the zwitterionic hydrogel tablet reached a higher degree of swelling than the non-zwitterionic hydrogel. The greater swelling implies that the zwitterionic hydrogel must have a larger mesh size than the non-zwitterionic hydrogel.

2.2 Measurement of Young's modulus

2 g of hydrogel microparticles (5.65 g PSB, 0.25 g BIS, 3.0 g F127DA, 5 ml DTPA-AA (0.25 M), 4.5 ml ethanol, and 0.5 ml PI) are prepared using an off-the-shelf micro-cross [3]. A TA instruments DHR-3 rheometer with parallel plate geometry (20 mm Peltier steel plate) was used in axial compression mode to axially strain the particles up to a maximum axial force/loading of 1 N. Care was taken to ensure that the particles formed a tightly packed monolayer between the plates, completely filling the gap, and all fluid was drained using a wipe immediately prior to measurement. Rapid measurement and the use of a solvent trap ensures that the hydrogel microparticles are fully hydrated during measurement. The force and gap between the rheometer plate and stage were recorded at equal intervals over multiple compression-relaxation cycles at equilibrium, and used to obtain the stress-strain plots shown in supplementary figure S13. The Young's modulus of the monolayer is obtained as the slope of the best-fit lines in supplementary figure S13 (1.27 ± 0.17 MPa). Performing the measurement over multiple cycles mimics practical operation in a packed bed, and using multiple samples allows us to capture variation across batches.

2.3 Synthesis of GMA-IDA

GMA-IDA is synthesized as described previously[14]. In brief, 6.055 g IDA (iminodiacetic acid) is dissolved in 50 ml 2M sodium hydroxide solution in water. 6.821 ml GMA (glycidyl methacrylate) is added dropwise, and the mixture is allowed to react with constant stirring in the dark at room temperature for 6 h. The reaction is confirmed using 1H-NMR spectroscopy (see supplementary figure S16).

2.4 Synthesis of GMA-Alg

Based on a modified version of a previously described procedure[15], 2% (w/v) solution of sodium alginate (Alg) was prepared in 200 ml DI water, and 11 ml of GMA was added with constant

stirring. The mixture was heated to 60°C and 100 mg sodium hydroxide was added to catalyze the reaction. The mixture was allowed to react for 4 hours, and then poured into 600 ml of cold 200-proof ethanol in which the reacted GMA-Alg precipitates. GMA-Alg is collected by centrifugation and vacuum filtration, and then frozen at -20°C and dried in a lyophilizer over 4 days. The final solid is pale yellow to white in color and ground into a powder and used for subsequent experiments. The reaction is confirmed using 1H-NMR spectroscopy (see supplementary figure S16).

2.5 Protocol information for HPLC

The HPLC-MS is operated in negative polarization mode for BPA concentration measurements, and positive polarization mode for EDOL and NOL concentration measurements. We use a gradient combining water (A) and methanol (B) mobile phases, each containing 0.1% formic acid. The gradient is shown below in table 6, in positive polarization mode. In negative polarization mode, we operate the HPLC in isocratic mode with 10.0% B. Table 7 shows the peak locations (m/z), retention times, and limits of detection for all three organic micropollutants used in this study.

Time (min)	% B
0.00	15.0
6.00	25.0
26.00	85.0
31.00	85.0
35.00	15.0
42.00	15.0

Table 6 | HPLC-MS mobile phase gradient for operation in positive polarization mode to detect EDOL and NOL.

Micropollutant	Ionization mode	Retention time (min)	Peak location (m/z)	Limit of detection (ppb)
EDOL	Positive	29.5	297.2	10
BPA	Negative	3.0	227.0	10
NOL	Positive	25.5	145.1	10

Table 7 | Analytical data for the quantification of organic micropollutant concentrations.

2.6 SEM-EDS Analysis

200 PSB-BIS/DTPA-AA/F127DA microparticles were soaked in 1 ml of 10 g/L lead nitrate solution with constant shaking for 1 day. Samples were extracted and coated with a 5 nm carbon

conductive layer prior to imaging. Scanning electron microscopy images were recorded using a Zeiss Merlin High-resolution SEM with an EDX probe. Energy-dispersive X-ray spectroscopy for elemental mapping was performed at 20 kV and elemental peaks for lead were fit using the APEX software.

3. Supplementary Figures

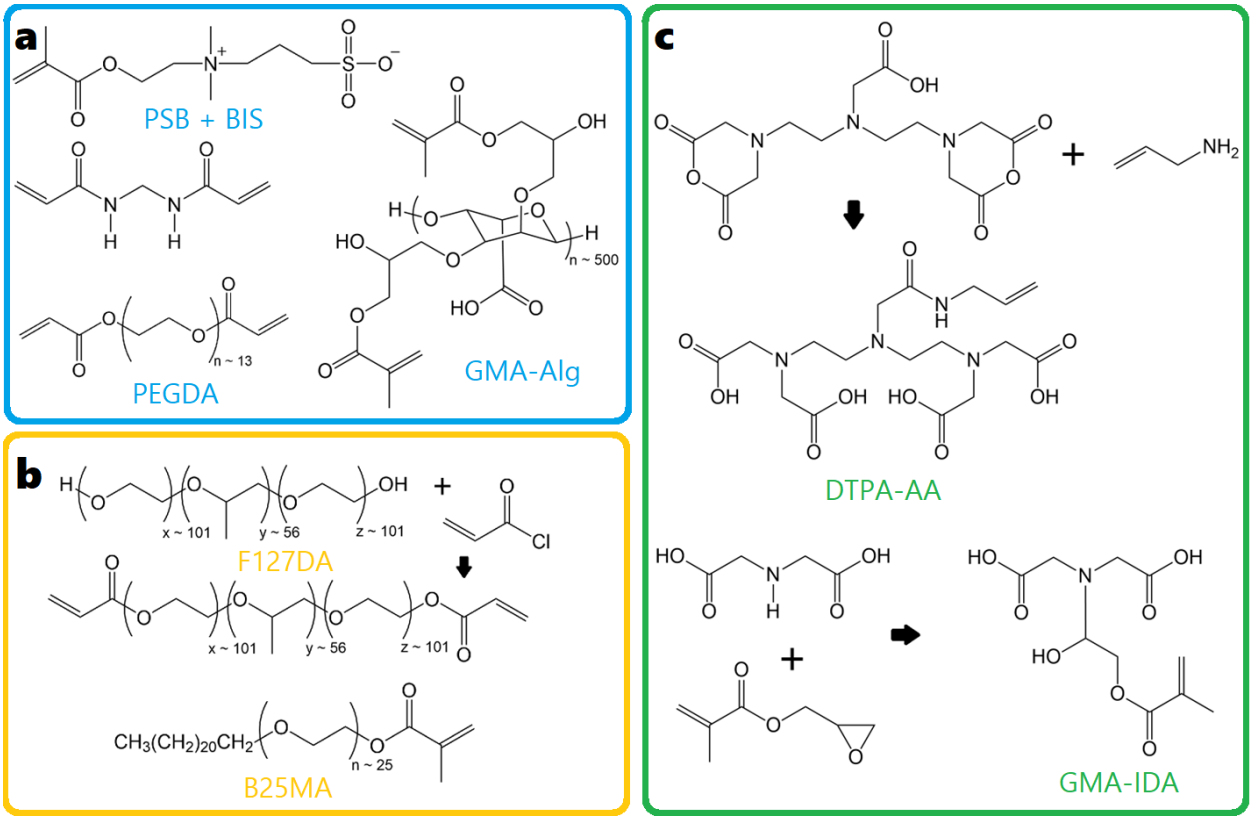

Fig. S1 | Chemical structures of monomers used to prepare hydrogel absorbents in this study. **a,** Chemical structures of monomers and crosslinkers used to make the hydrogel backbone. **b, c,** Chemical structures and synthesis pathways from commercially available precursor of the surfactants (**b**) and chelating agents (**c**) used in this study. Note that in (**a**), carboxylic acid groups in GMA-Alg have pKa around 3-4 [16], and at typical operating conditions (pH = 5-7), possess a negative charge (COO^-) and associated positive counterion. Further, in (**c**), allylamine may attack any of the carboxylic acid/acid anhydride sites on the DTPA-DA molecule to produce analogous structures of DTPA-AA, which are all functionalized with a double bond to enable their incorporation into a polymeric hydrogel, and can chelate metal ions. The stochiometric ratio of allylamine to DTPA-DA is set so that 1.15 sites per molecule are functionalized.

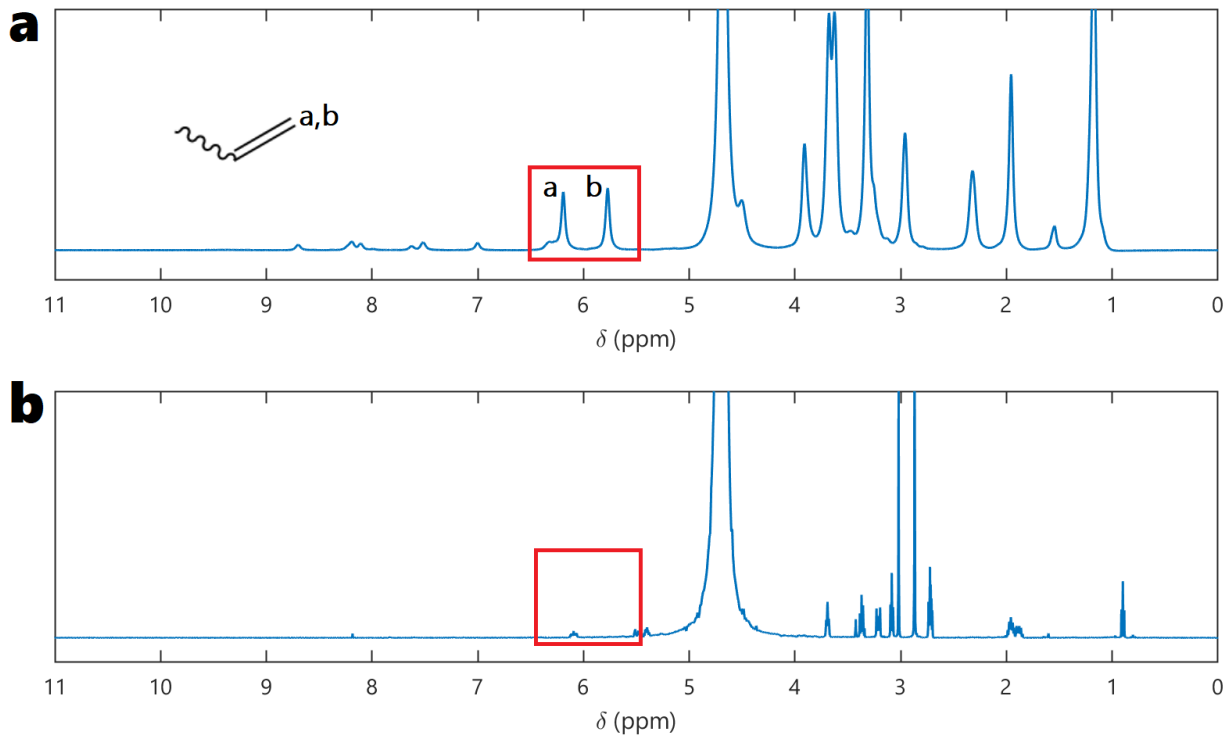

Fig. S2 | NMR spectra showing disappearance of acrylate peaks, indicating complete conversion of reactants during the polymerization process. a, PSB+BIS/DTPA-AA/F127DA monomer solution before polymerization, with acrylate peaks shown in the red box. Also present are urea by-products from the synthesis of DTPA-AA (1-4 ppm). **b,** The same solution, after polymerization, washing, and digestion in 14 M sodium hydroxide solution at 80°C for 3 days. Washing eliminates the urea by-product (loss of peaks in the 1-4 ppm region), while digestion release the individual monomers back into solution, enabling the use of traditional (non-solid state) 1H-NMR. The absent acrylate peaks indicate complete conversion during the polymerization process, implying that the surfactant and chelating agents are bound to the hydrogel matrix. This procedure has been described in prior work [1]. NMR assignment shown in inset.

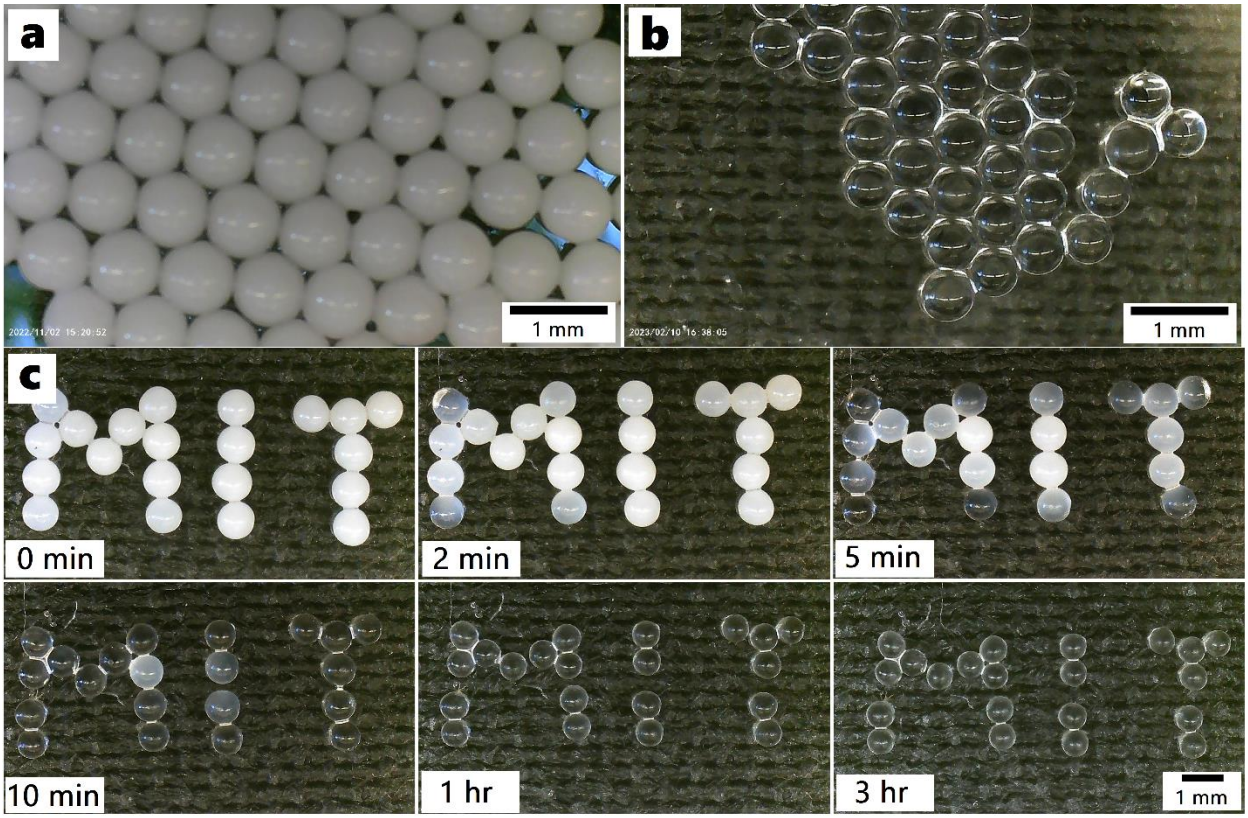

Fig. S3 | Effect of micelles on optical properties of zwitterionic hydrogel microparticles. a, b, Zwitterionic hydrogel microparticles (PSB) immediately after synthesis, with (**a**) and without (**b**) micelle-forming F127DA. The micelles have sufficient optical contrast relative to the hydrogel to scatter light when gelled close to each other, making the micelle-laden microparticles (**a**) opaque, unlike the microparticles without micelles (**b**). **c,** The loss of microparticle opacity as they are dried in air. Drying results in loss of water that is necessary to hold the self-assembled micelles together. It is possible to reverse this loss of opacity by adding water to the dried microparticles. The microparticles are seen to lose ~50% of their volume during drying, indicating a very porous internal structure. (**a, b, c**) indicate that micelles exist in their self-assembled form within the polymerized hydrogel microparticles.

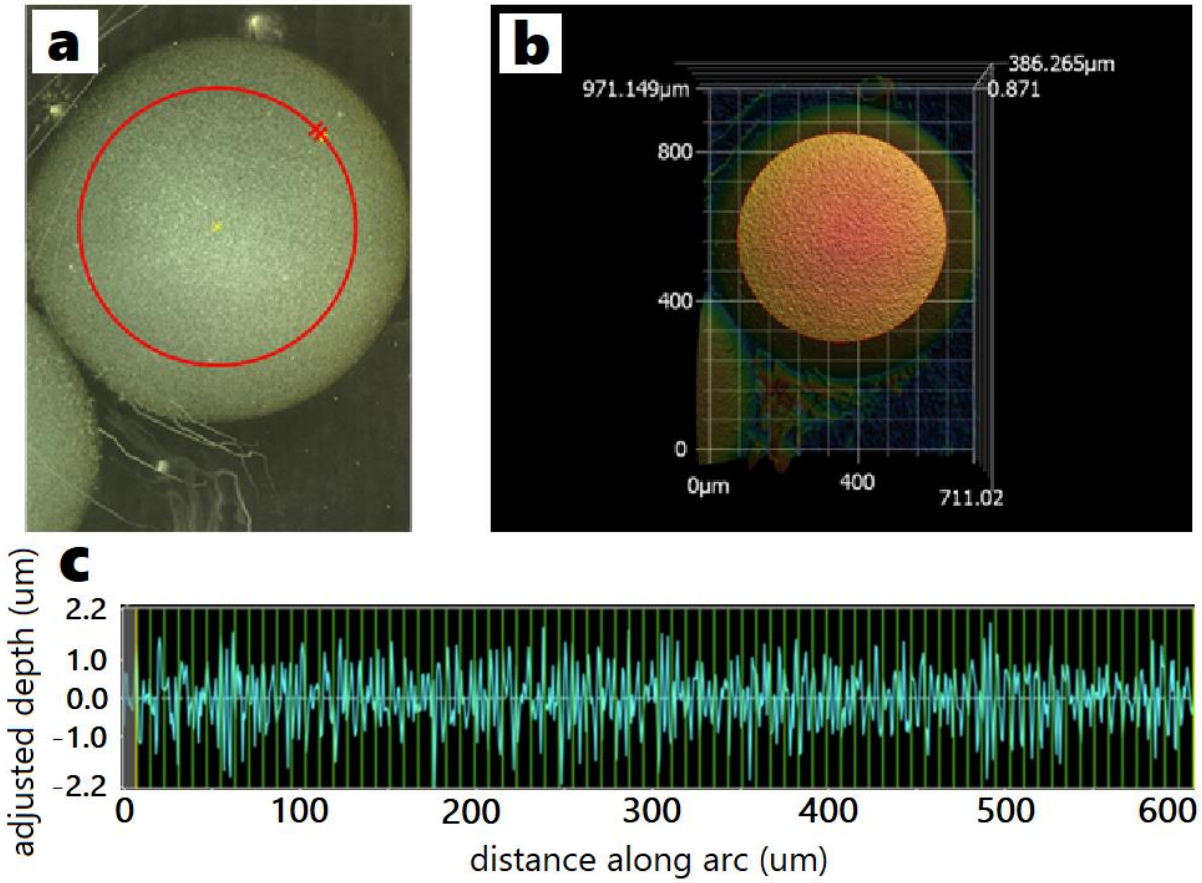

Fig. S4 | Surface morphology of zwitterionic hydrogel particles. a, Image of a zwitterionic hydrogel microparticle obtained using a light microscope. **b,** Image of the same particle using a Keyence VK-X250 laser scanning confocal microscope, showing a heatmap indicating depth. **c,** The roughness profile along the circle marked in red in (**a**) and (**b**), showing the relative smoothness of the hydrogel surface relative to the particle size (~700 um).

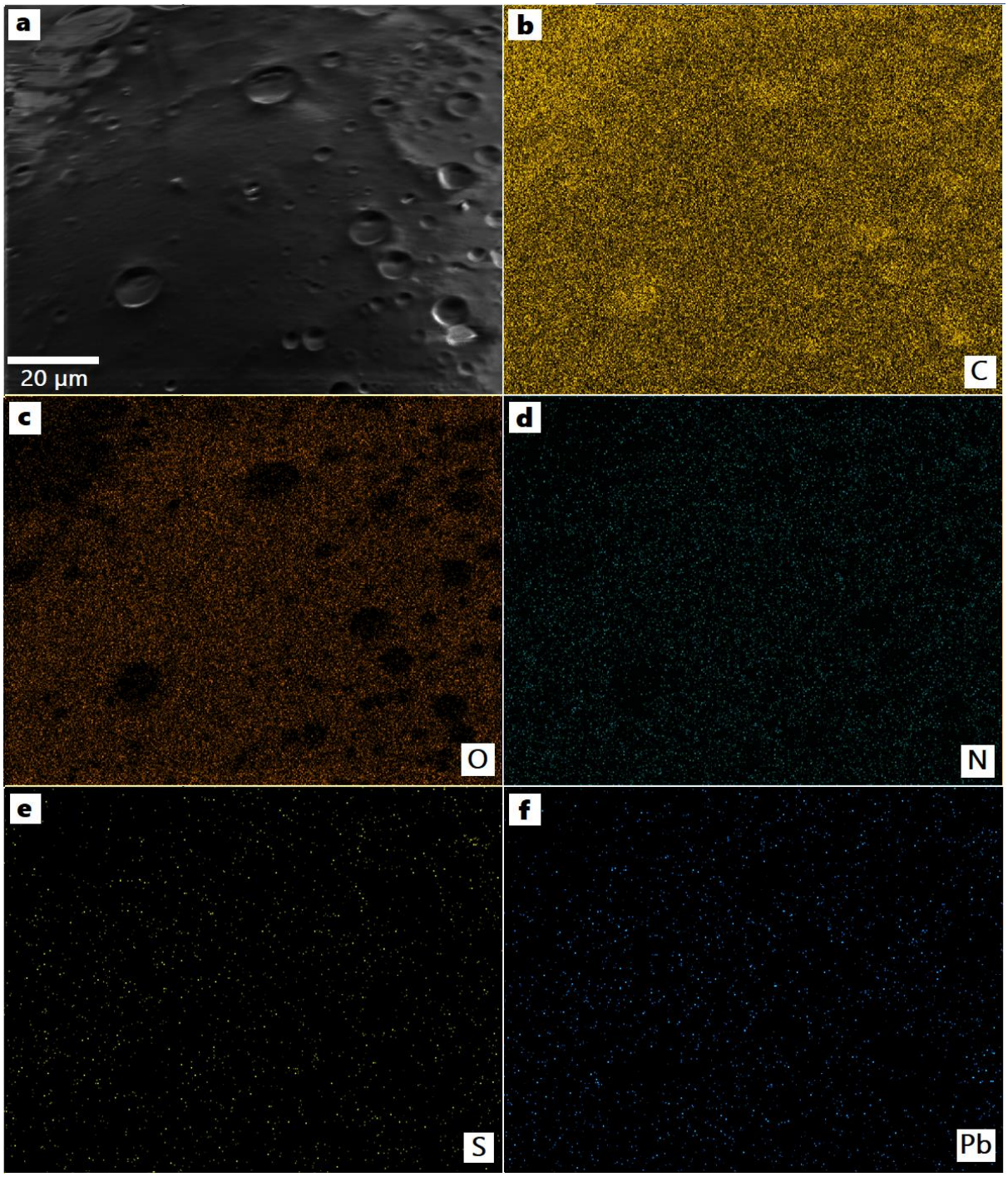

Fig. S5 | SEM-EDS elemental maps of a PSB/DTPA-AA/F127DA multifunctional zwitterionic hydrogel microparticle used to absorb lead from water. a, SEM image of the surface undergoing elemental mapping. **b-f,** Elemental maps of carbon, oxygen, nitrogen, sulfur, and lead, indicating uniform distribution inside the material. Sample preparation and analysis is described in supplementary information 2.6. Scale bars are the same for all images. Craters in (**a**) are an artefact of the carbon coating process for imaging and show up in (**b**) and in (**c**) in the form of oxygen depletion.

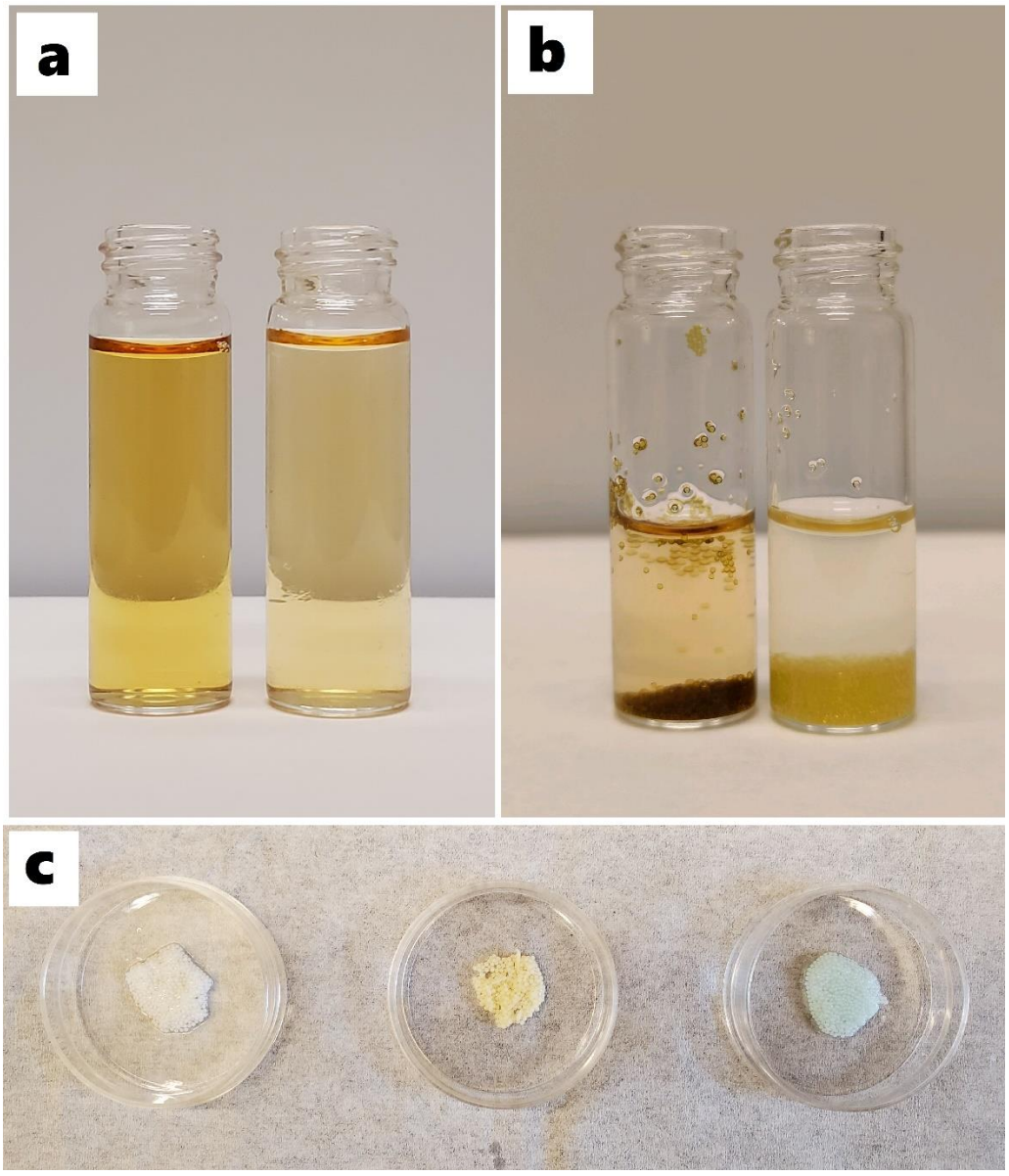

Fig. S6 | Images showing the use of PSB/DTPA-AA/F127DA multifunctional hydrogel microparticles to treat high concentration solutions of metal ions. a, b, 50 g/l (left) and 1 g/l (right) solutions of iron before (**a**) and after (**b**) treatment. Hydrogel microparticles settle to the bottom of the vial under the influence of gravity. Note the increased darkness of the hydrogel microparticles due to the significantly higher concentrations inside the particles relative to the supernatant. **c,** Hydrogel color after treating 1 g/l solutions of lead, iron, and copper (left to right).

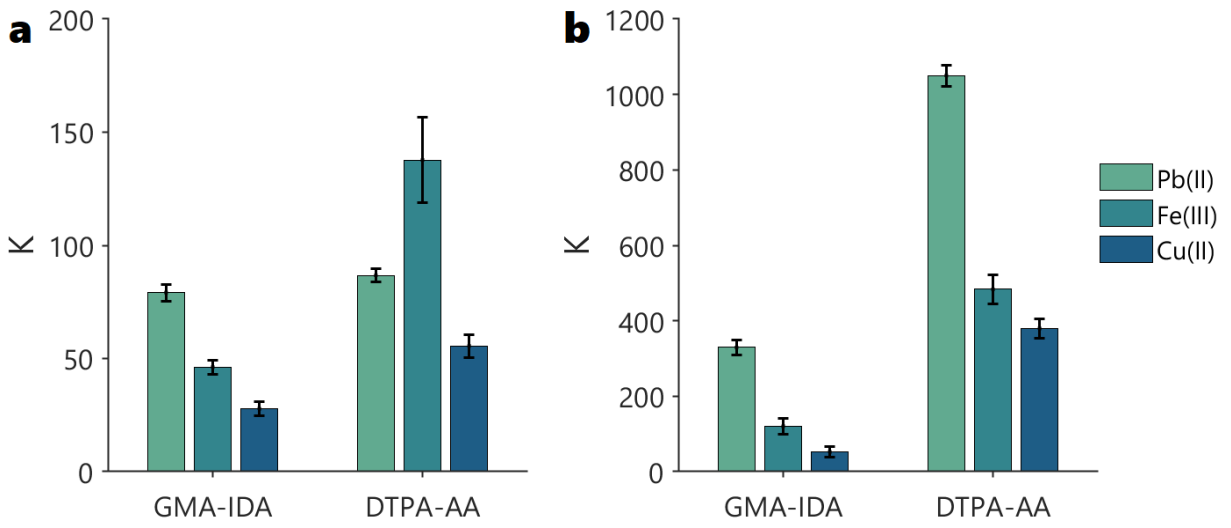

Fig. S7 | Comparison of ion-chelating selectivities of non-zwitterionic and zwitterionic hydrogels when functionalized with different chelating agents. a, b, Partition coefficients for the elimination of lead, iron, and copper ions by non-zwitterionic PEGDA (**a**) and zwitterionic PSB (**b**), each functionalized with either GMA-IDA or DTPA-AA. Due to the low affinity of PEGDA for metal ions, the chelating agent controls selectivity, while the high affinity of PSB for metal ions hides the selectivity of the chelating agent. Also see the relative quantities of various functional agents in supplementary information 1.2. Reported partition coefficient data are obtained as slopes of linear isotherms fit to data (n = 8) available in supplementary information 5. Error bars reflect the 95% confidence intervals associated with this fit.

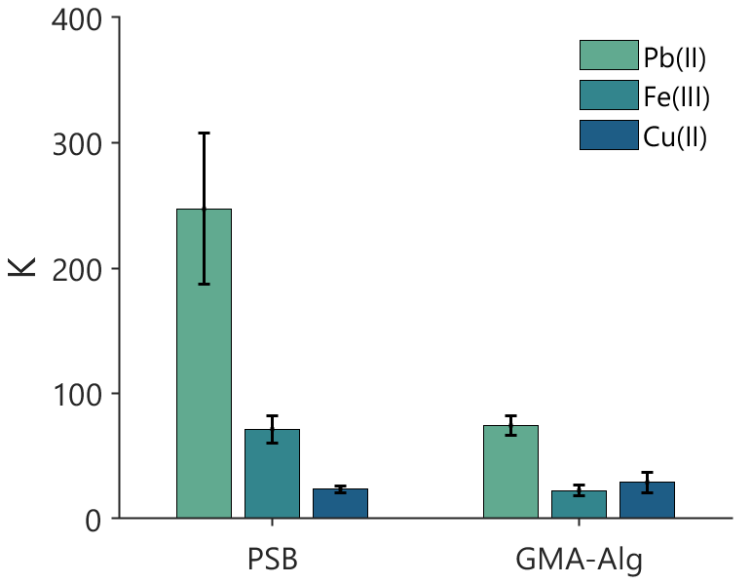

Fig. S8 | Comparison of partition coefficients for the uptake of lead, iron, and copper ions by zwitterionic PSB hydrogels, and non-zwitterionic egg-shell structure-forming alginate (GMA-Alg) hydrogels. The selectivity of GMA-Alg to specific metals is consistent with prior work [17]. Also see supplementary information 1.3. Reported partition coefficient data are obtained as slopes of linear isotherms fit to data (n = 8) available in supplementary information 5. Error bars reflect the 95% confidence intervals associated with this fit.

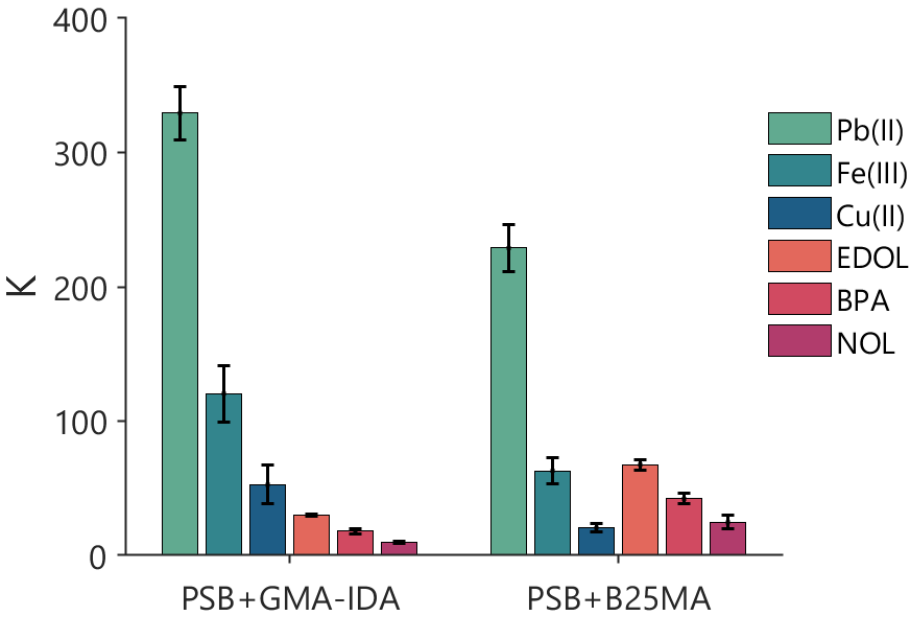

Fig. S9 | Partition coefficients for zwitterionic hydrogels prepared with alternate surfactants and chelating agent. Partition coefficients for PSB hydrogels functionalized either with chelating agent GMA-IDA or surfactant B25MA, demonstrating the versatility of the zwitterionic hydrogel platform. Structures of GMA-IDA and B25MA are shown in supplementary figure S1. Reported partition coefficient data are obtained as slopes of linear isotherms fit to data (n = 8) available in supplementary information 5. Error bars reflect the 95% confidence intervals associated with this fit.

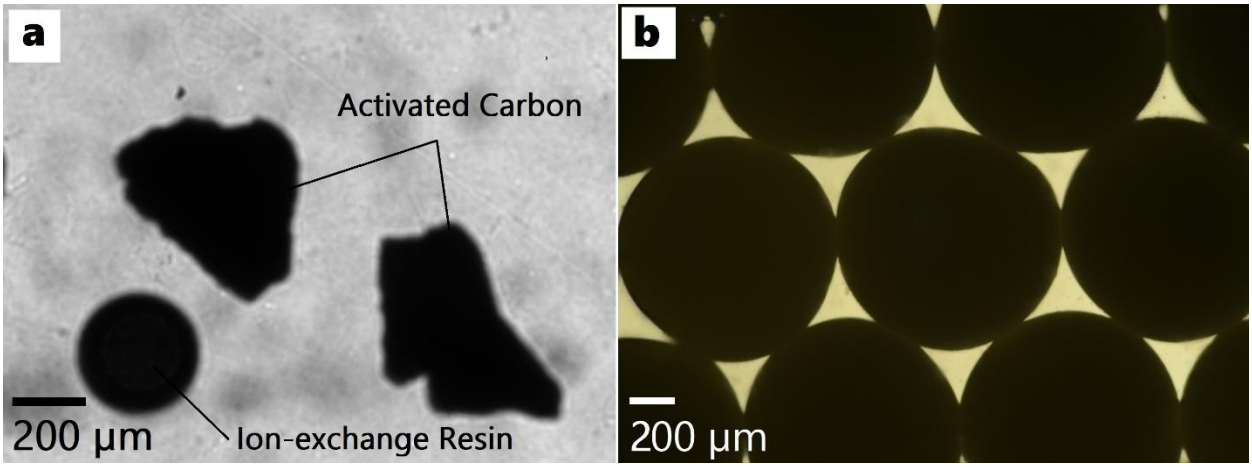

Fig. S10 | Relative sizes of (a) commercial activated carbon/ion-exchange resin and (b) hydrogel particles. Hydrogel particles have faster elimination kinetics despite their larger sizes.

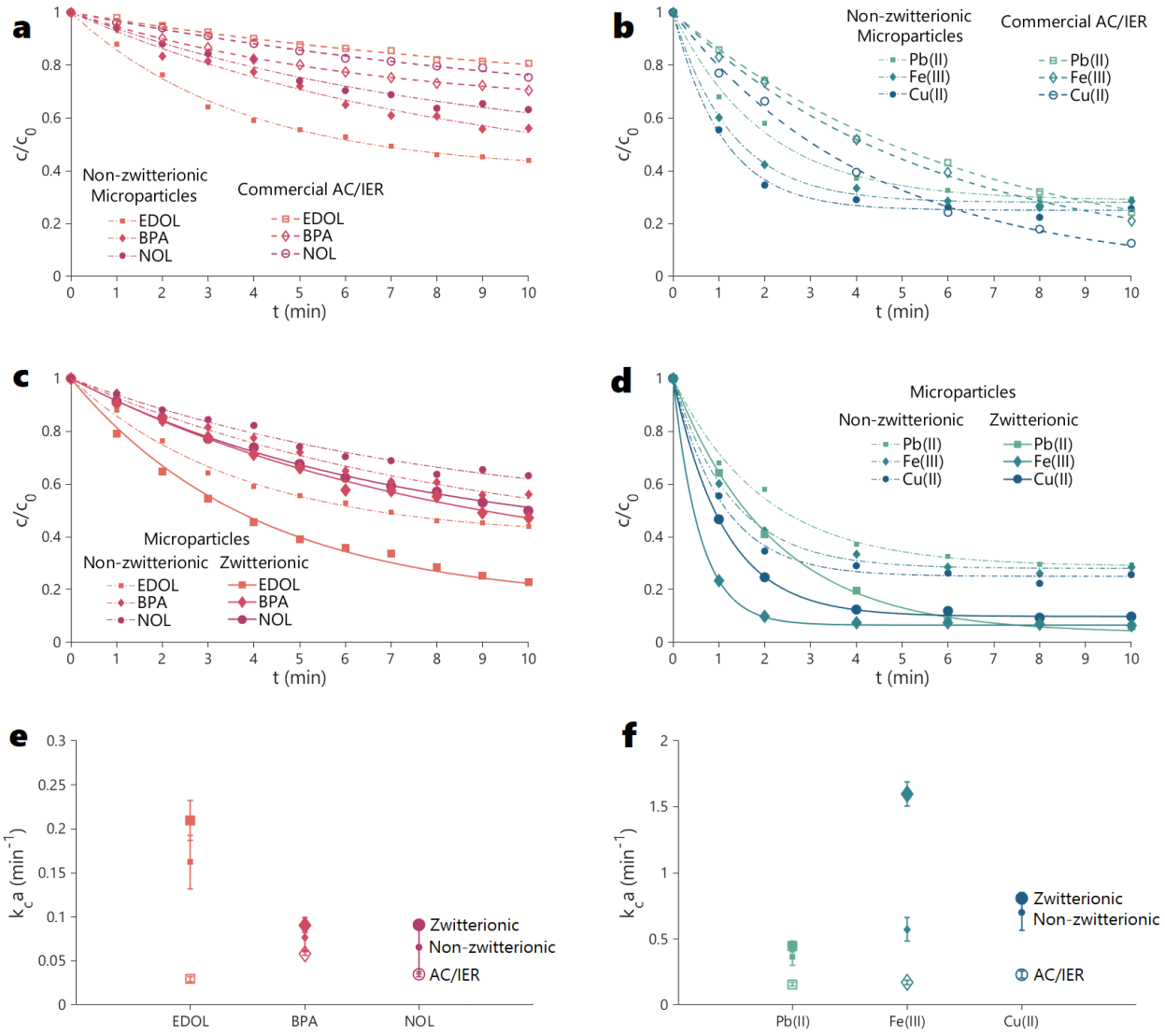

Fig. S11 | Micropollutant uptake kinetics by non-zwitterionic PEGDA/DTPA-AA/F127DA hydrogels, compared with uptake by zwitterionic PSB/DTPA-AA/F127DA hydrogels and commercial adsorbents. a, b, Uptake kinetics of non-zwitterionic microparticles compared to commercial materials, demonstrating that non-zwitterionic microparticles also remove micropollutants more rapidly than commercial adsorbents. **c, d,** Uptake kinetics comparison of non-zwitterionic microparticles with zwitterionic microparticles, both having the same crosslinking density. Zwitterionic microparticles show faster uptake, suggesting that that zwitterions enhance transport by increasing swelling, and therefore mesh size (supplementary information 1.4 and 2.1). Note in (**b**,**d**) that the total capacity of metal absorption is significantly reduced by removing zwitterions that also chelate metals (also see supplementary information 1.2) **e, f,** Mass transfer coefficients computed as in the main manuscript, as described in supplementary information 1.6. Non-zwitterionic microparticles have mass transfer coefficients that lie between zwitterionic microparticles and commercial adsorbents. Error bars in (**e,f**) reflect 95% confidence intervals obtained by fitting supplementary equation 1.6.4 to the data in (**a-d**). **e**: n = 11, **f**: n = 7

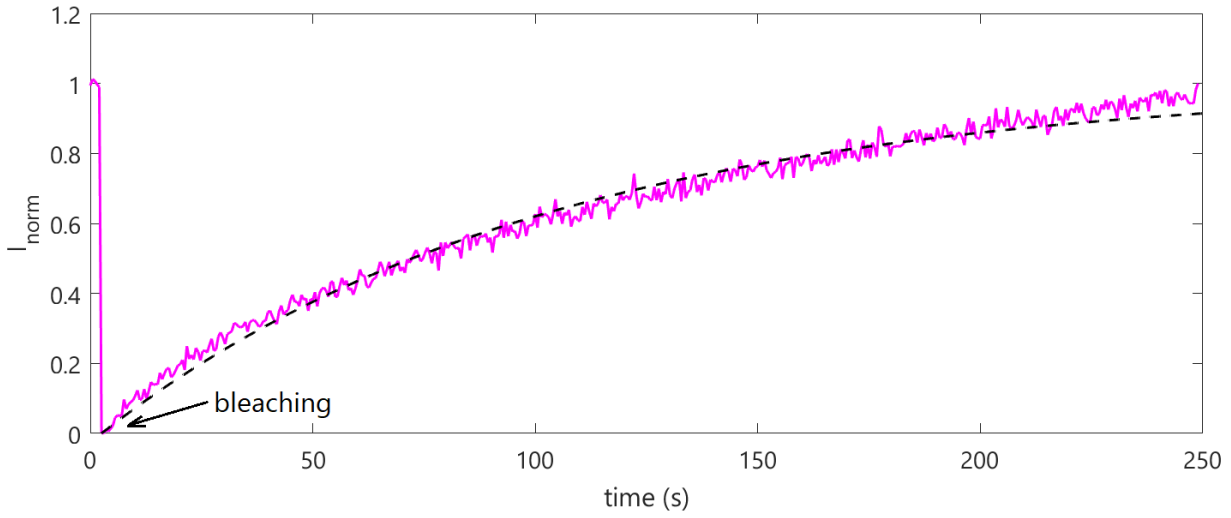

Fig. S12 | Normalized FRAP intensity over time (magenta), also showing the best-fit exponential described in supplementary discussion 1.5 and the bleaching event.

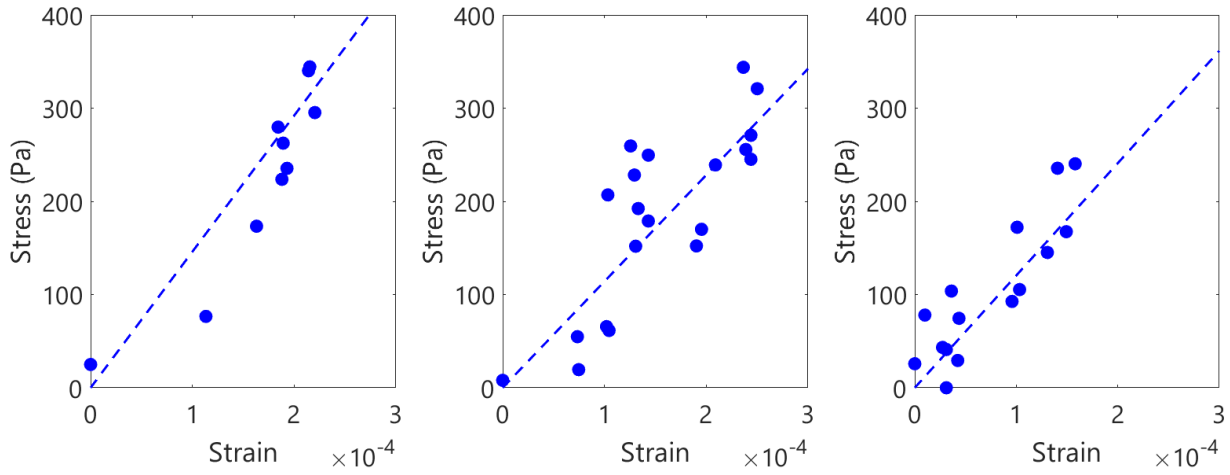

Fig. S13 | Stress-strain curves for the determination of Young's modulus of 3 samples of PSB/DTPA-AA/F127DA multifunctional zwitterionic hydrogels. Young's moduli are measured as described in supplementary methods section 2.2.

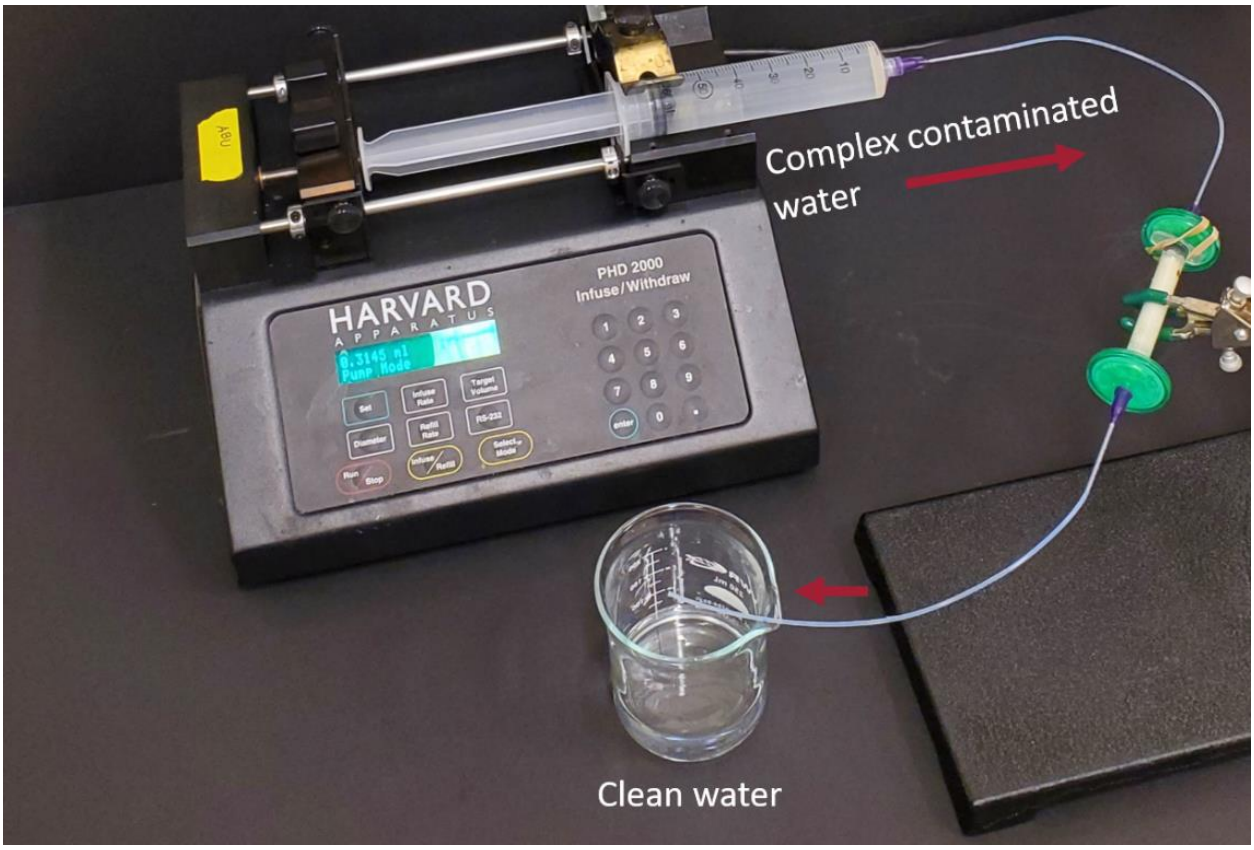

Fig. S14 | Photograph showing a continuous water treatment setup using a multifunctional zwitterionic hydrogel microparticle-filled packed bed.

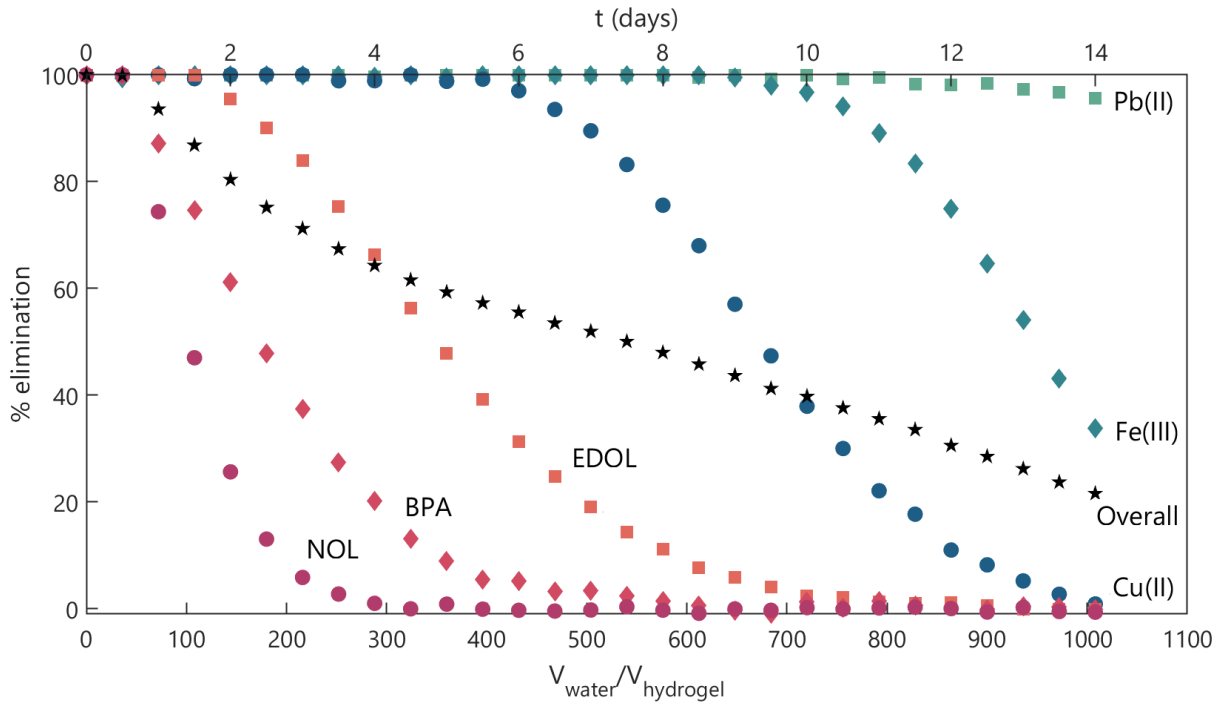

Fig. S15 | Elimination of micropollutants from a complex mixture containing 400 ppb of each micropollutant using the packed bed setup in supplementary figure S12. Breakthrough can be predicted as described in supplementary information 1.8.

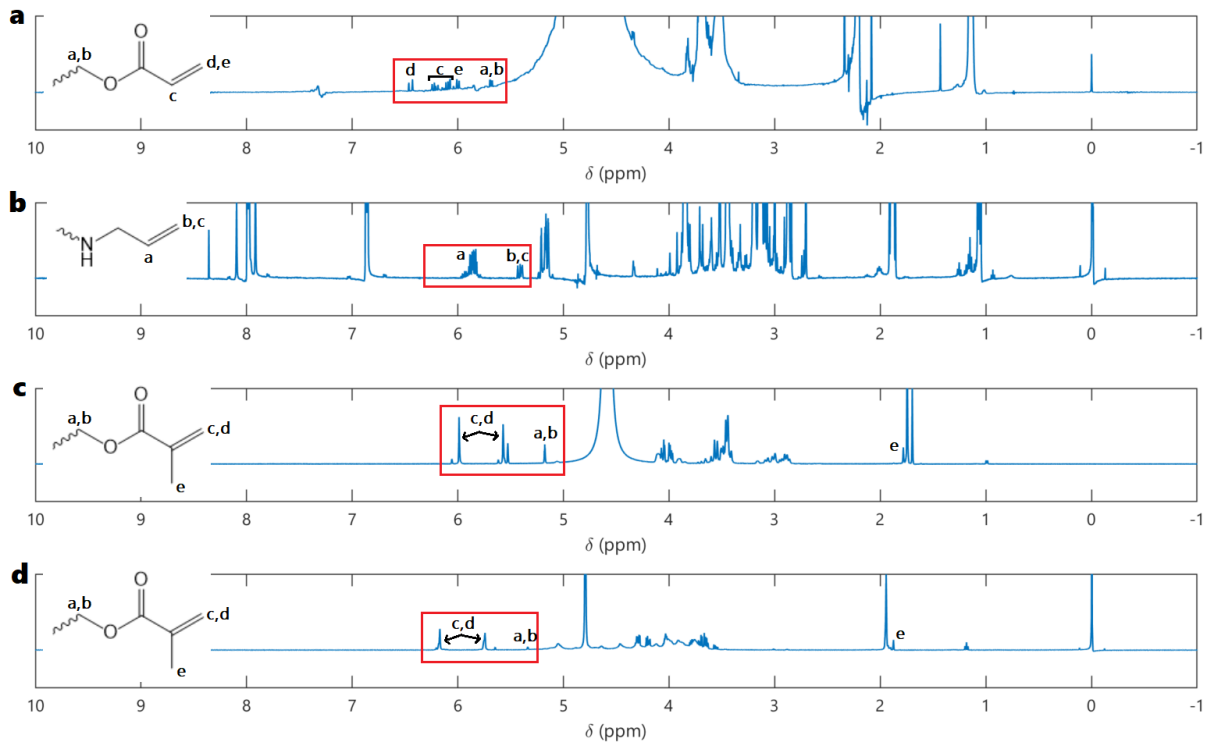

Fig. S16 | 1H-NMR spectra confirming the acrylation of precursors for incorporation into hydrogel microparticles. a, F127DA, showing the peaks corresponding to the acrylate moiety in the red box. **b,** DTPA-AA, showing the peaks corresponding to the acrylate moiety in the red box. **c,** GMA-IDA, showing the peaks corresponding to the methacrylate moiety on the GMA unit in the red box. **d,** GMA-Alg, showing the peaks corresponding to the methacrylate moiety in the red box. NMR assignments shown in insets.

4. Supplementary Video

Video SV1 | Use of hydrogel microparticles to rapidly treat a solution of iron at very high concentration (10 g/l).

5. Supplementary Source Data

Full_Data_Set.xlsx | Compositions and internal and supernatant concentrations of micropollutants for experiments performed as a part of this study.

6. References

[1] D. Gokhale, I. Chen, and P. S. Doyle, 'Micelle-Laden Hydrogel Microparticles for the Removal of Hydrophobic Micropollutants from Water,' *ACS Appl. Polym. Mater.*, **4(1)**, 746-754 (2022)

[2] K. Y. Lee and D. J. Mooney, 'Alginate: properties and biomedical applications,' *Prog. Polym. Sci.*, **37(1)**, 106-126 (2012)

[3] H. Kakita and H. Kamishima, 'Some properties of alginate gels obtained from algal sodium alginate,' *J. Appl. Phycol.*, **20**, 543-549 (2008)

[4] T. Canal and N. A. Peppas, 'Correlation of mesh size and equilibrium degree of swelling of polymeric networks,' *J. Biomed. Mater. Res.*, **23(10)**, 1103-1237 (1989)

[5] N. R. Richbourg and N. A. Peppas, 'The swollen polymer network hypothesis: Quantitative models of hydrogel swelling, stiffness, and solute transport,' *Prog. Polym. Sci.*, **105**, 101243 (2020)

[6] Y. Tsuji, X. Li, and M. Shibayama, 'Evaluation of Mesh Size in Model Polymer Networks Consisting of Tetra-Arm and Linear Poly(ethylene glycol)s,' *Gels*, **4(2)**, 50 (2018)

[7] J. M. Uruena, A. A. Pitenis, R. M. Nixon, K. D. Schulze, T. E. Angelini, and W. G. Sawyer, 'Mesh Size Control of Polymer Fluctuation Lubrication in Gemini Hydrogels,' *Biotribology*, **1-2**, 24-29 (2015)

[8] E. M. Staffer, M. A. Lackey, D. M. Griffin, S. Kishore, G. N. Tew, and S. R. Bhatia, 'SANS Study of Highly Resilient Poly(ethylene glycol) Hydrogels,' *Soft Matter*, **10(12)**, 1905-1916 (2014)

[9] S. M. Russell and G. Carta, 'Mesh Size of Charged Polyacrylamide Hydrogels from Partitioning Measurements,' *Ind. Eng. Chem. Res.*, **44(22)**, 8213-8217 (2005)

[10] M. Kang, M. Andreani, and A. K. Kenworthy, 'Validation of Normalizations, Scaling, and Photofading Corrections for FRAP Data Analysis,' *PLoS One*, **10(5)**, e0127966 (2015)

[11] P. C. Carman and R. A. W. Haul, 'Measurement of diffusion coefficients,' *Proc. R. Soc. A*, **222(1148)**, 109-118 (1953)

[12] J. Crank, 'The Mathematics of Diffusion,' 2nd ed., section 6.3.3, pp. 93, Clarendon Press, Oxford (1975)

[13] Philadephia Water Department: Gallons Used Per Person Per Day. https://water.phila.gov/pool/files/home-water-use-ig5.pdf. Accessed: 2023-09-01

[14] A. J. Macbeth, Z. Lin, and J. M. Goddard, 'General method for emulsion polymerization to yield functional terpolymers,' *MethodsX*, **7**, 101110 (2020)

[15] X. Wang, T. Hao, J. Qu, C. Wang, and H. Chen, 'Synthesis of thermal polymerizable alginate-GMA hydrogel for cell encapsulation,' *J. Nanomater.*, **2015(5)**, 5, (2015)

[16] N. L. Francis, P. M. Hunger, A. E. Donius, B. W. Riblett, A. Zavaliangos, U. G. K. Wegst, and M. A. Wheatley, ‘An ice-templated, linearly aligned chitosan-alginate scaffold for neural tissue engineering,’ *J. Biomed. Mater. Res. A*, **101(12)**, 3493-3503 (2013)

[17] H. Zhang, J. Cheng, and Q. Ao, ‘Preparation of Alginate-Based Biomaterials and Their Applications in Biomedicine,’ *Mar. Drugs*, **19(5)**, 264 (2021)